PHYSICAL REVIEW B **95**, 155106 (2017)

Evidence for antiferromagnetic-type ordering of f-electron multipoles in $\mathrm{PrIr_2Zn_{20}}$

Kazuaki Iwasa[*]
Frontier Research Center for Applied Atomic Sciences & Institute of Quantum Beam Science,
Ibaraki University, Tokai, Naka, Ibaraki 319-1106, Japan

Keisuke T. Matsumoto
Graduate School of Science and Engineering, Ehime University, Matsuyama 790-8577, Japan

Takahiro Onimaru and Toshiro Takabatake
Department of Quantum Matter, Graduate School of Advanced Sciences of Matter, Hiroshima University,
Higashi-Hiroshima 739-8530, Japan

Jean-Michel Mignot and Arsen Gukasov
Laboratoire Léon Brillouin, CEA-CNRS, CEA/Saclay, 91191 Gif sur Yvette, France

(Received 25 December 2016; revised manuscript received 15 March 2017; published 4 April 2017)

Neutron diffraction measurements conducted under applied magnetic fields evidence the ordered structure of $\mathrm{PrIr_2Zn_{20}}$ below approximately 0.1 K. A two-channel (orbital) Kondo effect is expected to act within the non-Kramers doublet ground state of the Pr $4f$ electrons of this material in cubic symmetry. Antiferromagnetic reflections are clearly induced under the influence of applied magnetic fields, which are characterized by the propagation vector $\boldsymbol{q} = (1/2,1/2,1/2)$. This result indicates antiferromagnetic-type ordering of the Pr f-electron multipoles. The Γ_3-type quadrupole, O_2^2, is the dominant order parameter deduced from the observed magnetic structure factor. We also discuss the entanglement of various finite-magnitude multipoles up to third rank, which are relevant to the low-energy crystalline-electric-field split levels in this material.

DOI: 10.1103/PhysRevB.95.155106

I. INTRODUCTION

Electronic multipole degrees of freedom have been found to play an important role in the physical properties of a growing number of strongly correlated f-electron systems. The long-range order or dynamics of (electric) quadrupoles [1,2], (magnetic) octupoles [3], and even higher-order multipoles result in a variety of novel phenomena [4]. In the case of non-Kramers ions with the f^2 configuration, a cubic crystalline electric field (CEF) can produce a doublet ground state with symmetry Γ_3, which carries no dipole magnetic moment but possesses higher-order multipole degrees of freedom. For example, the compound $\mathrm{PrPb_3}$ exhibits no long-range magnetic dipole order, but develops an incommensurate order of electric quadrupole moments below 0.4 K [5,6]. The ordered structure of the nonmagnetic quadrupole was determined by magnetic-field-induced dipoles detected by a neutron diffraction technique, which was explained by the group-theory classification of the relationship between the ordered multipoles and the induced dipoles [7]. In addition, it has been argued that the Γ_3 state of the f^2 configuration can yield the so-called “two-channel Kondo effect” [8], in which the f-electron doublet ground state becomes overscreened by conduction electrons, possibly leading to a new type of non-Fermi (NFL) liquid regime properties. Consequently, systems containing Pr^{3+} or U^{4+} ions, both of which exhibit a f^2 configuration, have been the subject of numerous studies on such multipole-driven phenomena.

In this connection, the $\mathrm{Pr}Tr_2X_{20}$ compounds (Tr: Transition metal element, X: Al or Zn) crystallizing in the cubic $\mathrm{CeCr_2Al_{20}}$-type structure (space group: $Fd\bar{3}m$, No. 227), are of particular interest [9,10]. The Al-based compounds $\mathrm{Pr}Tr_2\mathrm{Al}_{20}$ ($Tr =$ Ti and V) have been studied previously [11]. In $\mathrm{PrTi_2Al_{20}}$, inelastic neutron scattering (INS) measurements have confirmed that its CEF scheme presents a Γ_3 ground state [12]. Ferro-type quadrupole order has been evidenced by neutron diffraction measurement. $\mathrm{PrV_2Al_{20}}$ has been reported to exhibit two successive phase transitions at $T_{\mathrm{Q}} = 0.75$ K and $T^* = 0.65$ K, which are attributed to the quadrupole and octupole ordering [13]. Both compounds become superconducting, with critical temperatures $T_{\mathrm{C}} = 0.2$ K and 0.05 K, respectively. In $\mathrm{PrTi_2Al_{20}}$, an enhancement of the superconducting phase has been observed in response to an applied pressure [14–16]. The magnetic susceptibilities of both compounds also exhibit a $-\sqrt{T}$ dependence between approximately 3 and 20 K, thereby indicating a NFL state. Their electrical resistivities above 100 K show a $-\ln T$ dependence, indicative of a conventional magnetic Kondo effect. Between 3 and 20 K, the resistivity of $\mathrm{PrV_2Al_{20}}$ exhibits a NFL behavior characterized by $\sqrt{T}$, following a maximum in the vicinity of 40 K, while $\mathrm{PrTi_2Al_{20}}$ exhibits a conventional metallic T^2 dependence. Another member of this family, $\mathrm{PrNb_2Al_{20}}$, has also been suggested to host NFL phenomena associated with the Γ_3 ground state and strong c-f hybridization [17,18].

In this paper, we focus on the isomorphous Zn-based compound $\mathrm{PrIr_2Zn_{20}}$ (lattice constant: 14.2729 Å [10]), which looks promising because evidence for the Γ_3 CEF doublet ground state has been reported from an INS study [19]. A sharp peak in the temperature dependence of its specific heat at $T_{\mathrm{Q}} = 0.11$ K [20] has been ascribed to the onset of antiferro-quadrupole (AFQ) order, based on ultrasonic

---

[*] kazuaki.iwasa.ifrc@vc.ibaraki.ac.jp

measurements [21]. T_Q depends slightly on magnetic fields, and the ordered phase disappears at 5 and 10 T applied along the [0 0 1] and [1 1 0] axes, respectively. However, the order parameter of this phase has not yet been identified using microscopic techniques. The electrical resistivity decreases at T_Q with decreasing temperature and drops to zero at the superconducting transition occurring at $T_C = 0.05$ K [22]. The coexistence of the AFQ order and the superconducting state suggests a possible interplay between the quadrupole fluctuations and the superconducting pair formation. Contrary to the expected splitting of the twofold degenerated Γ_3 doublet in response to the electronic ordering, the magnetic entropy at T_Q is only 20% of $R \ln 2$, where R is the gas constant. Very recently, anomalous behaviors have been observed at approximately 5 T in magnetic fields applied along the [0 0 1] axis: kinks in the electrical resistivity and the specific heat show [23] large softening of the elastic modulus, $(C_{11} - C_{12})/2$ (where the $C_{\alpha\beta}$ are elastic constants) [21], and enhancement by approximately a factor of 100 of the Seebeck coefficient with respect to its zero-field value [24]. These field-induced anomalies are most likely caused by the strong interaction between the $4f$-electron multipoles and the conduction electrons. For the Zn-based materials, the $4f$-electron part of the specific heat divided by temperature, C/T, behaves as $-\ln T$, and an upward convex curve in the electrical resistivity is visible within the narrow temperature range $0.2 < T < 0.8$ K [10]. The most striking discovery is that the temperature dependencies of the various physical quantities obey a universal scaling function for the NFL behavior, which is derived from the quadrupolar Kondo lattice model [23,25].

To reveal the origin of the anomalous behavior of $\mathrm{PrIr_2Zn_{20}}$, the order parameter and its temperature and magnetic-field dependences have been investigated. Based on neutron diffraction measurement, we show that $\mathrm{PrIr_2Zn_{20}}$ undergoes antiferromagnetic-type multipole ordering characterized by the propagation vector $\boldsymbol{q} = (1/2,1/2,1/2)$ and that the Γ_3-type quadrupole moment O_2^2 is the dominant order parameter.

II. EXPERIMENTAL DETAILS

Single-crystalline samples of $\mathrm{PrIr_2Zn_{20}}$ were synthesized using the melt-growth method. These samples were sliced into thin plates with approximate dimensions of $3\times3\times0.5$ mm^3, in order to reduce the absorption effect of Ir nuclei for thermal neutrons. Four or five sample plates were co-aligned, and neutron diffraction measurements were performed on the lifting-detector diffractometer (the lift angle: $-5 \leqslant \nu \leqslant +20^\circ$) installed at the 6T2 beam hole of the Orphée reactor at Laboratoire Léon Brillouin, France. A pyrolytic graphite monochromator was used to select a neutron wavelength of 2.4 Å, and pyrolytic graphite filters were installed in order to eliminate higher-order contaminations. A square-hole collimator with dimensions of 20×15 mm^2 and a circular-hole collimator with a diameter of $\phi 20$ mm were installed along the incident and scattered beams, respectively. A cryomagnet equipped with a dilution refrigerator insert was used to cool the sample to 40 mK and to apply vertical magnetic fields of up to 6 T along the $[\bar{1}10]$ and [0 0 1] axes of the co-aligned sample.

III. RESULTS AND ANALYSIS

A. Measurements for magnetic fields applied along $[\bar{1}10]$ axis

Figure 1(a) shows scan profiles across the scattering vector $\boldsymbol{Q} = (1,1,-1)$ at various measurement temperatures and magnetic fields applied along the $[\bar{1}10]$ axis. No distinct profile change for this reflection appears on crossing the phase boundary deduced from the previous studies, within the resolution of the experiment. This result indicates no structural change at T_Q. We measured magnetic-field induced ferromagnetic component at the $\boldsymbol{Q} = (2,2,0)$ reflection, of which the nuclear intensity is small. As shown in Fig. 1(b), the magnetic intensity at 40 mK enhances with increasing magnetic fields. This result is reproduced by a quadratic function of the magnetic field, as shown by solid line. Such behavior is similar to a paramagnetic response to the applied magnetic field. Figure 1(c) shows scan profiles across $\boldsymbol{Q} = (0.5,0.5,1.5)$ at a measuring temperature of 50 mK. The data measured at 50 mK and in a magnetic field of 5 T applied along the $[\bar{1}10]$ axis exhibits a peak (red open circles), while the intensity disappears in a zero magnetic field (blue solid squares) even below T_Q determined from the specific-heat data. Figure 1(d) shows the T dependence of the integrated intensity of the rocking scan across $\boldsymbol{Q} = (0.5,0.5,-1.5)$ at a fixed magnetic field of 5 T. The intensity begins to increase below 120 mK, which corresponds to T_Q consistent with the specific-heat measurement [20] and the results of ultrasonic studies [21]. Figure 1(e) shows the magnetic-field dependence of the same reflection measured at a fixed temperature of 40 mK. The induced antiferromagnetic (AFM) peak intensity is enhanced with increasing magnetic field. The data follow a quadratic function of the magnetic field, as shown by the solid line. These results indicate that a primary order parameter is nonmagnetic multipole of the $4f$ electrons in $\mathrm{PrIr_2Zn_{20}}$, because the AFM structure characterized by the reduced wave vector $\boldsymbol{q} = (1/2,1/2,1/2)$ grows smoothly from zero magnitude with increasing magnetic fields. We will also discuss that various multipoles associated with the low-energy CEF levels can be entangled in the ordered phase of $\mathrm{PrIr_2Zn_{20}}$, in contrast to the single-multipole ordering in $\mathrm{PrTi_2Al_{20}}$.

The measured squared structure factors F_N^2 of the fundamental nuclear reflections were evaluated from the integrated intensity of the rocking scans divided by the Lorentz factor. In order to compare the results with the calculated F_N^2, we assumed the same atomic fractional coordinates for $\mathrm{PrIr_2Zn_{20}}$, which have not determined yet, as those determined for $\mathrm{EuTa_2Al_{20}}$ [26]. Figure 1(f) shows the measured squared structure factors F_N^2 as a function of the calculated F_N^2. The measured data are roughly proportional to the calculated F_N^2, as indicated by the black line in the figure determined by a linear least-squares fitting procedure. The scatter of the data is due to the asymmetrically co-assembled thin-plate samples and the neutron-absorption effect, which depends strongly on the sample rotation angle with respect to the incident and outgoing neutron beams. This fitting result is used below, as a scale to convert the measured intensities to the absolute values of the structure factors for the induced AFM reflections.

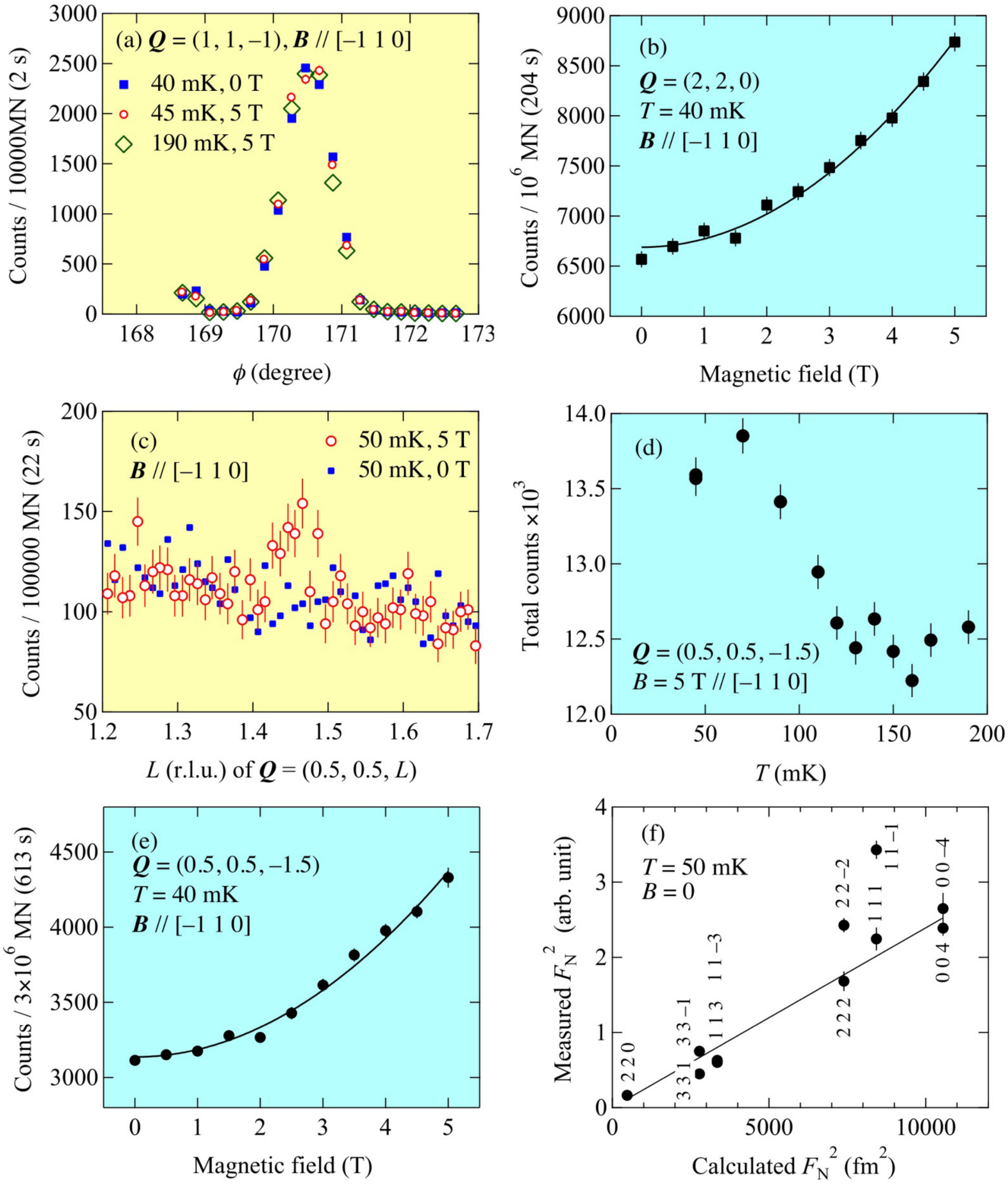

FIG. 1. Measured results under magnetic fields applied along the $[\bar{1}10]$ axis are shown. (a) Rocking profiles, where ϕ is the crystal-rotation angle, at $\boldsymbol{Q} = (1,1,-1)$ measured at various temperatures and magnetic-field values. (b) Measured magnetic-field dependence of the peak intensity at $\boldsymbol{Q} = (2,2,0)$ at a fixed temperature of 40 mK (symbols). The solid line is a quadratic least-squares fit as a function of the magnetic field. (c) Measured scan profiles along $[0.5, 0.5, L]$ reciprocal space line for magnetic fields $B = 0$ (blue solid squares) and 5 T (open red circles) magnetic fields applied along the $[\bar{1}10]$ axis, at a fixed temperature of 50 mK. (d) Temperature dependence of integrated intensity of a scan across $\boldsymbol{Q} = (0.5,0.5,-1.5)$ for a fixed magnetic field of 5 T. (e) Measured magnetic-field dependence of the peak intensity at $\boldsymbol{Q} = (0.5,0.5,-1.5)$ at a fixed temperature of 40 mK (symbols). The solid line is a quadratic least-squares fit as a function of the magnetic field. (f) Experimental versus calculated squared structure factors F_{N}^2 of fundamental nuclear reflections. The solid line shows the linear least-squares fit.

We observed similar magnetic-field-induced reflections at several points in reciprocal space, for example, for $\boldsymbol{Q} = (0.5,0.5,-1.5)$ and $(0.5,0.5,2.5)$, as shown in Figs. 2(a) and 2(b), respectively. On the other hand, it is noteworthy that some of the superlattice reflections indexed by $\boldsymbol{q} = (1/2,1/2,1/2)$ do not appear in the ordered phase. As shown in Figs. 2(c) and 2(d), no peaks were detected at $\boldsymbol{Q} = (1.5,1.5,-0.5)$ and $(1.5,1.5,1.5)$, respectively, under the field of 5 T. The fundamental nuclear peaks for $\boldsymbol{Q} = (1,1,1)$ and $(2,2,2)$ were confirmed to be observed during the whole measurement sequence, and the instrument setup (the crystal alignment or the reciprocal-space definition and the diffractometer accuracy) was sufficiently conserved. This fact ensures that no peak appears at $\boldsymbol{Q} = (1.5,1.5,1.5)$ even at the finite magnetic fields, since its reciprocal-space position is located just between these two fundamental reflections.

In Table I, the measured squared structure factors, F_{exp}^2, evaluated using the scale factor determined from the data shown in Fig. 1(f) are listed for various $\boldsymbol{Q} = (H,K,L)$ reflections together with their statistical errors, $\Delta F_{\mathrm{exp}}^2$. For the thirteen examined reflections, only five field-induced peaks were detected.

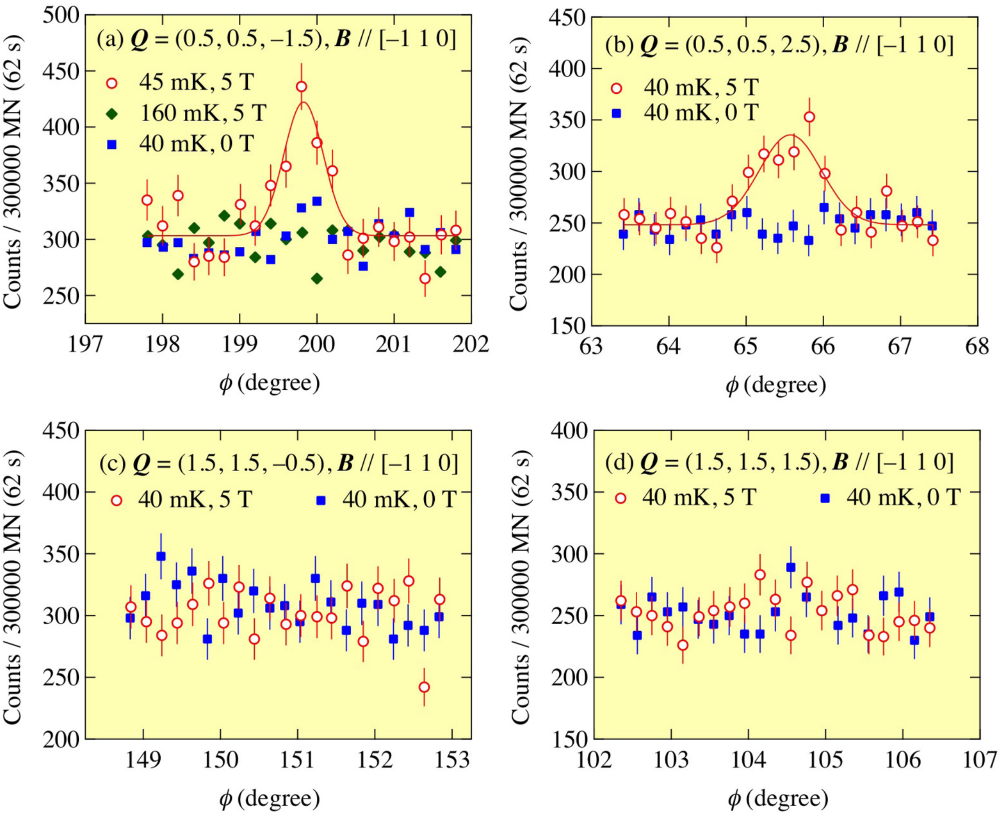

FIG. 2. Rocking profiles at selected reciprocal-lattice points characterized by $\boldsymbol{q} = (1/2,1/2,1/2)$. The measurements were conducted under a zero magnetic field (blue solid squares) and for a field of 5 T (red open circles) applied along the $[\bar{1}10]$ axis. The sample temperature was fixed to 40 mK. The data obtained at 160 mK and for a field of 5 T are also shown in frame (a) (green solid diamonds).

The characteristic magnetic structure factors are indispensable for determination of the order parameter. In particular, the null intensity at $\boldsymbol{Q} = (1.5,1.5,-0.5)$ and $(1.5,1.5,1.5)$ will be discussed in detail in order to identify which multipole plays a role in the ordered structures. As deduced later in the analysis part, the AFM-moment direction is perpendicular to the applied-field direction. This observed result cannot be explained only by the dipole and indicates the symmetry of the ordered multipoles, as discussed previously for CeB$_6$ [7]. Because the long-period structure in the ordered phase, we expect formation of domain structures characterized by $\boldsymbol{q} = (1/2,1/2,1/2)$ and $\boldsymbol{q} = (1/2,1/2,-1/2)$, which are equivalent for the $[\bar{1}10]$ axis along the magnetic fields. The domain formation will also be discussed in a forthcoming analysis part for calculation of magnetic-structure values.

TABLE I. Experimental results for the squared structure factors, $F^2_{\rm exp}$, in units of fm^2, along with their errors, $\Delta F^2_{\rm exp}$, for magnetic-field-induced reflections at $\boldsymbol{Q} = (H,K,L)$, measured at 40 mK and for a field of 5 T applied along the $[\bar{1}10]$ axis. Dashes indicate the absence of observed intensities. $F^2_{[111]}$ is the calculated result for the model of the AFM moment of $\pm(0.1,0.1,0.1)$ parallel to the [1 1 1] axis. $F^2_{O^0_2}$ and $F^2_{O^2_2}$ are calculated results for the pure O^0_2 and O^2_2 quadrupole orders, respectively. The induced magnetic dipole vectors are $\pm(-0.108,0.108,0)$ and $\pm(0.108,0.108,0)$, respectively.

H	K	L	$F^2_{\rm exp}$	$\Delta F^2_{\rm exp}$	$F^2_{[111]}$	$F^2_{O^0_2}$	$F^2_{O^2_2}$
0.5	0.5	1.5	15.4	5.7	0	0	0
0.5	0.5	−1.5	16.5	3.9	25.46	20.58	16.84
0.5	0.5	2.5	29.4	6.6	10.04	19.93	18.45
0.5	0.5	−2.5	7.2	5.5	0	0	0
1.5	−0.5	−0.5	18.7	5.1	25.46	5.61	16.84
0.5	−0.5	−1.5	–	–	0	0	0
1.5	1.5	0.5	–	–	0	0	0
1.5	1.5	−0.5	–	–	2.49	3.47	0.18
1.5	1.5	1.5	–	–	0	19.93	6.64
1.5	1.5	−1.5	–	–	0	0	0
1.5	−0.5	−1.5	–	–	0	0	0
1.5	0.5	−1.5	–	–	0	0	0
1.5	0.5	−0.5	–	–	0	0	0

B. Measurements for magnetic fields applied along [001] axis

Next, we conducted measurements in magnetic fields applied along the [0 0 1] axis. The rocking-curve profile for the $\boldsymbol{Q} = (4,0,0)$ fundamental reflection is shown in Fig. 3(a), which is composed of split peaks owing to imperfect orientation of crystals. However, because the fundamental-reflection intensities were sufficient, we could search the magnetic component induced by magnetic fields. As shown in Fig. 3(b), the ferromagnetic component superimposed on the $\boldsymbol{Q} = (2,2,0)$ was clearly observed again. We examined the field-induced AFM reflections at 19 individual $\boldsymbol{Q} = (H,K,L)$ positions corresponding to $\boldsymbol{q} = (1/2,1/2,1/2)$, in the ranges of indices

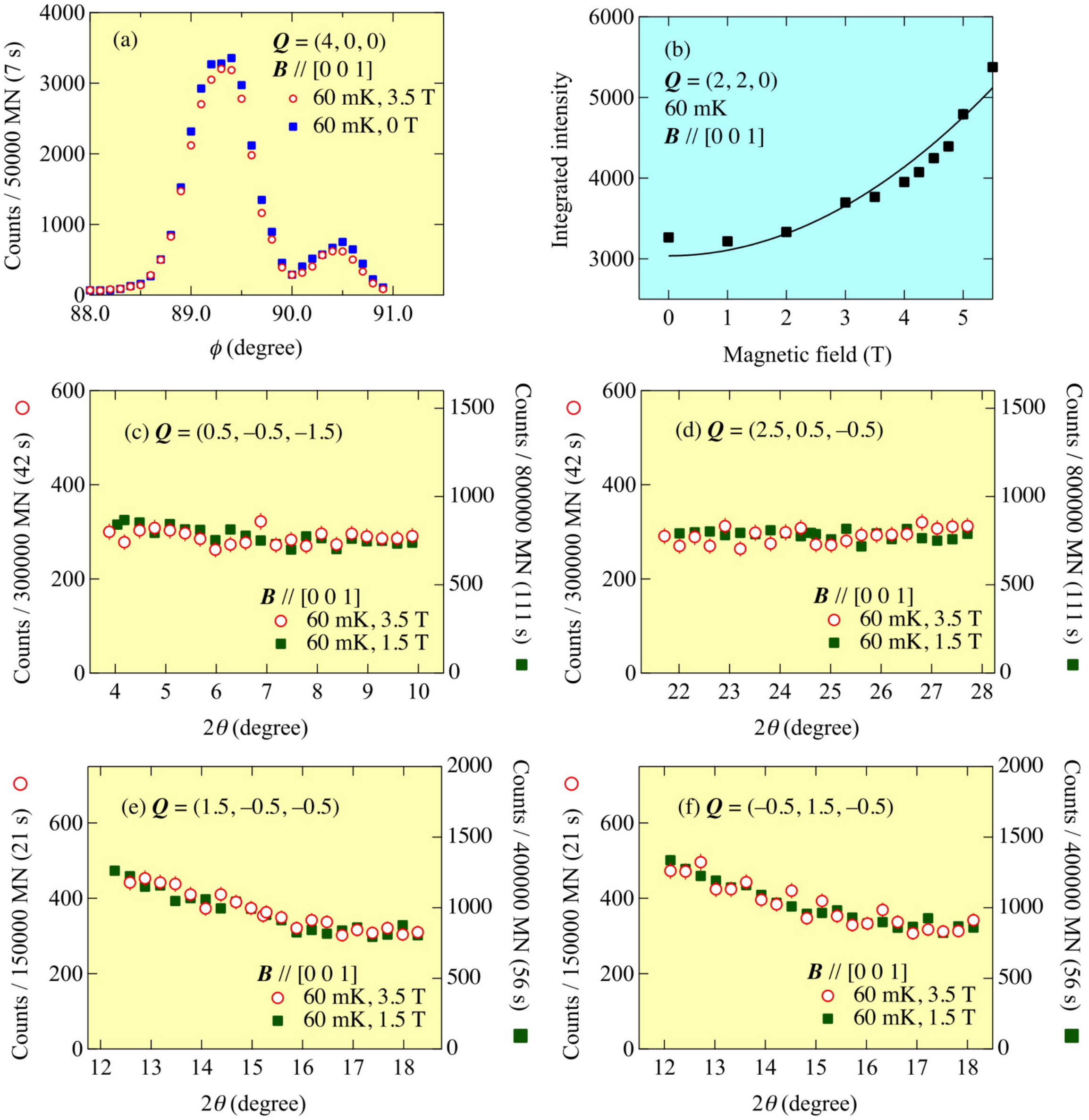

FIG. 3. (a) Rocking-curve scan profiles for $\boldsymbol{Q} = (4,0,0)$ in zero and magnetic field of 3.5 T at 60 mK. (b) Measured magnetic-field dependence of integrated intensity at $\boldsymbol{Q} = (2,2,0)$ at 60 mK (solid symbols). The solid line is a quadratic least-squares fitting result. (c)–(f) Scattering-angle 2θ scan profiles at selected reciprocal-lattice positions characterized by $\boldsymbol{q} = (1/2,1/2,1/2)$. The applied magnetic fields are 1.5 (green solid squares) and 3.5 T (red open circles) along the [0 0 1] axis. The sample temperature was fixed to 60 mK.

$-0.5 < H < 2.5$, $-0.5 < K < 2.5$, and $-1.5 < L < -0.5$. Measurements in magnetic fields of 1.5 and 3.5 T were performed at 60 mK in the ordered phase for the magnetic fields applied along the [001] axis, which was revealed in previous studies [20,21]. No induced AFM reflections were observed. Figures 3(c)–3(f) show selected scan profiles at $\boldsymbol{Q} = (0.5,-0.5,-1.5)$, $(2.5,0.5,-0.5)$, $(1.5,-0.5,-0.5)$, and $(-0.5,1.5,-0.5)$ as functions of the scattering angle, 2θ. The data sets obtained in the fields of 1.5 and 3.5 T for each $\boldsymbol{Q}$ exhibit flat or sloping intensities as a function of 2θ without magnetic-field dependencies. We also conducted scans along the high-symmetry directions in the reciprocal space, and no additional field-induced AFM reflection was observed. This result is very informative as regards identification of the ordered electronic state symmetry.

IV. DISCUSSION

A. Unit cell of ordered superstructure

The present experimental results indicate that no spontaneous magnetic-dipole ordering occurs in zero magnetic field, whereas the AFM structure is induced by the applied magnetic field along the $[\bar{1}10]$ axis. This observation can be ascribed to an antiferromagnetic-type ordering of nonmagnetic multipoles of the Pr $4f$ electrons in $\mathrm{PrIr_2Zn_{20}}$, which is similar to AFQ order investigated in $\mathrm{PrPb_3}$ [6].

In order to determine the ordered structure, we referred to the magnetic space groups for the $\boldsymbol{q} = (1/2,1/2,1/2)$ AFM structure available for the original space group, $Fd\bar{3}m$, which were obtained from the Bilbao Crystallographic Server (http://www.cryst.ehu.es/) [27]. We checked all of the magnetic subgroups under the original $Fd\bar{3}m$, and found that the $R_I\bar{3}c$ trigonal space group without the lattice-origin shift (maximal magnetic subgroup, No. 167.108 of the Belov-Neronova-Smirnova setting) is consistent with the Pr lattice with the finite AFM moments. The atomic-coordinate transformation from $Fd\bar{3}m$ to $R_I\bar{3}c$ preserves the Pr-ion locations, on which the $\boldsymbol{q} = (1/2,1/2,1/2)$ AFM structure superimposes to be consistent with the observed magnetic structure factors, as described in detail later. The transformation of the $R_I\bar{3}c$ with the lattice-origin shift of (0, 1/2, 0) fails to reproduce the Pr-ion lattice. The $R_I\bar{3}m$ (No. 166.102) space group reproduces the Pr sites, but these should not be occupied by magnetic moments. Further, the R_I32 (No. 155.48) space group, for example, gives a large value of magnetic structure factor for $\boldsymbol{Q} = (1.5,1.5,-0.5)$, which is not consistent with the observed result shown in Table I. After such a check for the magnetic subgroups, we take the $R_I\bar{3}c$ (No. 167.108) magnetic space group without the lattice-origin shift as a starting model to explain the observed superlattice reflections as well as the expected multipole ordering.

The magnetic unit cell for the $R_I\bar{3}c$ structure is hexagonal defined by the unit vectors $\boldsymbol{a}_R = (1/2,-1/2,0)$, $\boldsymbol{b}_R = (0,1/2,-1/2)$, and $\boldsymbol{c}_R = (2,2,2)$, while those for the original $Fd\bar{3}m$ are $\boldsymbol{a} = (1,0,0)$, $\boldsymbol{b} = (0,1,0)$, and $\boldsymbol{c} = (0,0,1)$. The Pr ions are located at the 8a Wyckoff positions (1/8, 1/8, 1/8) and (7/8, 7/8, 7/8) of the $Fd\bar{3}m$ structure, which corresponds to the fractional coordinates of $(0,0,z)_R$ and $(0,0,-z+1/2)_R$ with $z = 1/16$ for the 12c site in the hexagonal unit cell, where the subscript R indicates the coordinate with respect to the $R_I\bar{3}c$ unit cell. These atomic sites carry magnetic moments $\boldsymbol{M}_{\mathrm{AF}} = (0,0,M_z)_R$ and $(0,0,-M_z)_R$, respectively. The equivalent points are given by translational operations of $(0,0,0)_R+$, $(2/3,1/3,1/3)_R+$, $(1/3,2/3,2/3)_R+$, $(0,0,1/2)'_R+$, $(2/3,1/3,5/6)'_R+$, and $(1/3,2/3,1/6)'_R+$, where $'$ indicates inversion of the time-reversal symmetry for $\boldsymbol{M}_{\mathrm{AF}}$ with respect to the $\boldsymbol{c}_R$ axis. The AFM structure model is shown in Fig. 4 [28]. The Pr ions are represented by yellow balls, with $\boldsymbol{M}_{\mathrm{AF}}$ being indicated by red arrows parallel to the $\boldsymbol{c}_R$ axis and the cubic [1, 1, 1] axis. The thin lines in the left and right panels show the unit cells of the $R_I\bar{3}c$ magnetic structure and the $Fd\bar{3}m$ original crystal structure, respectively.

The squared magnetic structure factors were calculated for this AFM structure by assuming $\boldsymbol{M}_{\mathrm{AF}} = \pm(0.1,0.1,0.1) = \pm(0,0,0.1\sqrt{3})_R$ in units of μ_{B}/Pr. The results are listed in the $F^2_{[111]}$ column in Table I. The calculated results for the squared structure factors are of the same order of magnitude as those for the observed peaks, F^2_{exp}. It is noteworthy that many of the null-intensity $\boldsymbol{Q}$ positions are reproduced. The $F^2_{[111]}$ at $\boldsymbol{Q} = (0.5,0.5,-1.5)$ and $(0.5,0.5,2.5)$ are of the same order as the observed F^2_{exp}. The $F^2_{[111]}$ has nonzero value for $(1.5,1.5,-0.5)$, but this value is significantly smaller than the averaged uncertainty $\Delta F^2_{\mathrm{exp}}$. Thus, the calculated small magnitude is consistent with the null-intensity measurement result at $(1.5,1.5,-0.5)$. The calculated values of $F^2_{[111]}$ at $(0.5,0.5,1.5)$ and $(0.5,0.5,-2.5)$ are null, whereas nonzero magnitudes are obtained for the measured F^2_{exp}. However, these observed reflections are produced by a domain characterized by $\boldsymbol{c}_R = (2,2,-2)$, which should coexist with the domain characterized by $\boldsymbol{c}_R = (2,2,2)$ considered in the present calculation. Because both of these hexagonal unique axes are perpendicular to the applied magnetic fields, these domains should coexist with the same probability. The domain characterized by $\boldsymbol{c}_R = (2,2,-2)$ also gives a small calculated value of $F^2_{[111]}$ for $\boldsymbol{Q} = (1.5,1.5,0.5)$ in addition to those for $(0.5,0.5,1.5)$ and $(0.5,0.5,-2.5)$, whereas the calculated values for the other reflections are not affected by the domain formation. Thus, the hypothesized unit cell for the magnetic superstructure is in accordance with the observed peak intensities, and this model can serve as a starting point for the determination of the order parameter in the following section.

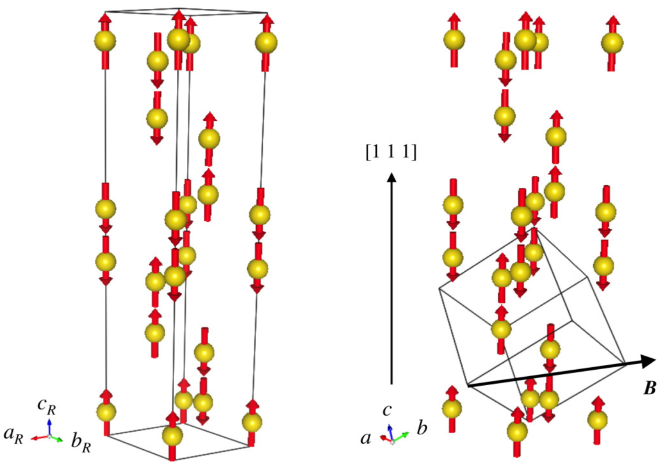

FIG. 4. Pr-ion sublattice (yellow balls) and model of magnetic-field-induced AFM structure. The magnetic moments $\boldsymbol{M}_{\mathrm{AF}}$ (red arrows) are parallel to the $\boldsymbol{c}_R$ axis of the unit cell (the polyhedron illustrated with solid lines) of the $R_I\bar{3}c$ superstructure (left panel), which corresponds to the [1 1 1] axis of the original cubic $Fd\bar{3}m$ structure (right panel). Note that this induced AFM structure is superimposed on the uniform ferromagnetic component along the magnetic-field direction $\boldsymbol{B}$, which is parallel to the $\boldsymbol{a}_R$ axis of the $R_I\bar{3}c$ hexagonal unit cell corresponding to the $[\bar{1}10]$ axis of the original cubic structure. These views were drawn using VESTA [28].

The AFM structure is comprised of a sequence of ↑↑↓↓ ferromagnetic (FM) planes along the hexagonal $\boldsymbol{c}_R$ axis (the cubic [1 1 1] axis). Because the Pr sublattice is the diamond-type structure in the face-centered cubic (fcc) lattice, all the distances between the Pr ions are equivalent. Therefore, the aforementioned FM planes are considered to be coupled equally with the neighboring planes. Note that such one-dimensional four-site periodic stacking arises in the Devil's staircase for the magnetic phase diagram based on the axial-next-nearest-neighbor-Ising (ANNNI) model [29]. The interactions between the nearest neighbors, J_1, and between the second-nearest neighbors, J_2, are FM and AFM, respectively. The ↑↑↓↓ structure becomes stable for $|J_2/J_1| > 0.5$, whereas other sequences are favorable for different $|J_2/J_1|$ regions, as well as different T values. Considering the correspondence between the ordered structure of $\mathrm{PrIr_2Zn_{20}}$ and the ANNNI model, the ordered-phase $\mathrm{PrIr_2Zn_{20}}$ may be dominated by the frustration effect in the multipole interactions.

B. Quadrupole order parameter

We consider the CEF level scheme for the Pr ions in $\mathrm{PrIr_2Zn_{20}}$, i.e., Γ_3 (0 meV)–Γ_4 (2.36 meV)–Γ_1 (5.67 meV)–Γ_5 (5.80 meV), as was determined in the previous INS study [19]. The Γ_3 doublet ground state carries the quadrupoles $O_2^0 = (2J_z^2 - J_x^2 - J_y^2)/2$ and $O_2^2 = (\sqrt{3}/2)(J_x^2 - J_y^2)$, where $\boldsymbol{J} = (J_x, J_y, J_z)$ is the dipole operator, and these quadrupoles are expected to constitute a primary order parameter.

The O_2^0 AFQ order implies an induced $\boldsymbol{M}_{\mathrm{AF}}$ parallel to the applied magnetic fields along the $[\bar{1}10]$ axis [7,30]. Therefore, the induced $\boldsymbol{M}_{\mathrm{AF}}$ would be approximately perpendicular to the $\boldsymbol{Q}$ vectors in the experimental setup with the detector tilt ν comprised between -5 and $+20^\circ$. Assuming an induced $\boldsymbol{M}_{\mathrm{AF}} = \pm(-0.108, 0.108, 0)\mu_{\mathrm{B}}/\mathrm{Pr}$, we calculated the squared structure factors, $F^2_{O_2^0}$, as listed in Table I. The calculated results for $(0.5, 0.5, -1.5)$ and $(0.5, 0.5, 2.5)$ are of the same order as the experimental results. However, the calculated result for $(1.5, 1.5, 1.5)$ has almost the same magnitude as those of $(0.5, 0.5, -1.5)$ and $(0.5, 0.5, 2.5)$, which is inconsistent with the present observation. Further, the calculated value for $(1.5, -0.5, -0.5)$ is smaller than for the other reflections, which also contradicts the experimental observation. Moreover, the most compelling result, i.e., the absence of detected induced AFM reflections under the influence of a magnetic field applied along the [0 0 1] axis (Fig. 3) is completely inconsistent with the O_2^0 AFQ order. That is, the O_2^0 AFQ order should be indicated by AFM reflections for the reflection points measured in the present study due to the magnetic dipoles induced along the applied magnetic-field direction [7,30]. Thus, we exclude the O_2^0 AFQ order from consideration as a primary order parameter of $\mathrm{PrIr_2Zn_{20}}$.

Next, the quadrupole O_2^2 is discussed. The O_2^2 AFQ order implies an induced $\boldsymbol{M}_{\mathrm{AF}}$ parallel to the [110] and perpendicular to the magnetic field applied along the $\boldsymbol{a}_R$ axis (the $[\bar{1}10]$ axis of the original cubic structure), as shown in Fig. 5 [7,30].

The red arrows are the induced AFM dipole components, and the colored balls correspond to the "up" and "down" sites of the ordered O_2^2 orbitals, respectively. We calculated the squared magnetic structure factors for the AFM reflections, with the results being listed in the $F^2_{O_2^2}$ column of Table I, by assuming $\boldsymbol{M}_{\mathrm{AF}} = \pm(0.108, 0.108, 0)\mu_{\mathrm{B}}/\mathrm{Pr}$. The calculated result at $(1.5, 1.5, 1.5)$ is approximately 35% of those at $(0.5, 0.5, -1.5)$ and $(0.5, 0.5, 2.5)$. This intensity ratio is significantly smaller than that for the O_2^0 AFQ case and is closer to the observation of the null intensity at $(1.5, 1.5, 1.5)$. The same values of $F^2_{O_2^2}$ are calculated for $(0.5, 0.5, -1.5)$ and $(1.5, -0.5, -0.5)$, and this result is consistent with the close values of F^2_{exp} for these reflections. Therefore, the O_2^2 AFQ order is in better agreement with the experimental result. Stronger support for the O_2^2 AFQ order is provided by the experimental evidence that no AFM structure is induced under the magnetic fields parallel to the [0 0 1] axis. Further, the quadrupole $O_2^2 = (\sqrt{3}/2)(J_x^2 - J_y^2)$ is irreducible for the rotation with respect to the [0 0 1] axis. This finding indicates that the same induced magnetic dipoles arise at all of the Pr sites in the O_2^2 AFQ ordered phase, and no AFM reflection appears. Therefore, it is concluded that the O_2^2 quadrupole is the primary order parameter in $\mathrm{PrIr_2Zn_{20}}$ [29].

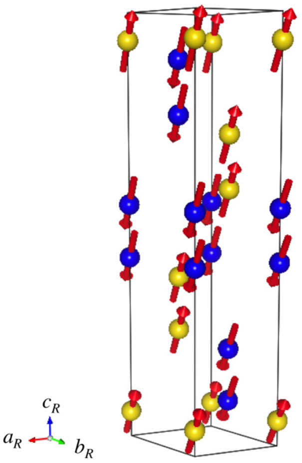

FIG. 5. Model of O_2^2 AFQ order at Pr-ion sublattice and magnetic-field-induced AFM structure. The magnetic fields were applied along the $\boldsymbol{a}_R$ axis of the unit cell (the polyhedron shown by solid lines) of the magnetic $R_I\bar{3}c$ structure, which corresponds to the $[\bar{1}10]$ axis in the original $Fd\bar{3}m$ cubic structure. The magnetic moments $\boldsymbol{M}_{\mathrm{AF}}$ (red arrows) are parallel to the [110] axis in the original cubic structure. The blue and yellow balls correspond to the "up" and "down" O_2^2 orbitals, respectively. Note that the actually induced AFM structure is superimposed with the uniform ferromagnetic component along the magnetic-field direction. This view was drawn using VESTA [28].

C. Multipole entanglement

In Sec. IV B, we concluded that the quadrupole O_2^2 is the most probable primary order parameter within the space defined by the Γ_3 CEF ground state. On the other hand, the calculated nonzero value of $F^2_{O_2^2}$ for $\boldsymbol{Q} = (1.5, 1.5, 1.5)$ is larger than the measuring errors, $\Delta F^2_{\mathrm{exp}}$, as listed in Table I. Therefore, the pure O_2^2 AFQ model is not in full accordance with the experimental result showing no intensity at $(1.5, 1.5, 1.5)$. Hence, we must investigate whether other ordered states beyond the pure O_2^2 AFQ order can describe the present experimental result more consistently. Hereafter, we discuss a multipole-ordered state which implies the field-induced AFM structure composed of the magnetic moments directed closer to the $\boldsymbol{c}_R$ axis as shown in Fig. 4, which gives $F^2_{[111]} = 0$ for $\boldsymbol{Q} = (1.5, 1.5, 1.5)$.

The role of the octupole $T_{xyz} = (\sqrt{15}/6)\overline{J_x J_y J_z}$, where the bar indicates the sum of the terms given by the cyclic permutation on $x, y,$ and z, should be considered. T_{xyz} becomes nonzero within the Γ_3 doublet CEF ground state and belongs to the Γ_1 irreducible representation of the T_d point group for the Pr-ion site, which is characteristic for the crystal structure of the 1–2–20 systems. In addition, considering the irreducible representations of multipoles, we can derive a Γ_1-symmetry multipole coupling term, $T_{xyz} J_x J_y J_z$, in the free-energy function for T_d [7,31]. The stable electronic state in the magnetic field applied along the twofold axis, which is determined by the differential of the free-energy function with respect to $J_x + J_y$, gives a finite magnitude of $T_{xyz}(J_x + J_y)J_z$. This result means that T_{xyz} accompanies an induced $\boldsymbol{M}_{\mathrm{AF}}$ parallel to the [0 0 1] axis (J_z) in magnetic fields along the twofold axis. Therefore, it is informative to examine how T_{xyz} contributes to the ordered structure of $\mathrm{PrIr_2Zn_{20}}$.

We also notice the relation between T_Q and the CEF splitting energy in the Pr 1–2–20 systems: the smaller the CEF splitting energy, the lower the T_Q value [10]. In particular, the Zn-based materials exhibit lower T_Q and smaller CEF splitting than those of $\mathrm{Pr}Tr_2\mathrm{Al_{20}}$. The order parameter of $\mathrm{PrTi_2Al_{20}}$ below $T_\mathrm{Q} = 2.8$ K in the magnetic field of 4 T applied along the [0 0 1] axis is the pure O_2^0 quadrupole [12]. The complicated ordered state of $\mathrm{PrIr_2Zn_{20}}$ described above is in marked contrast to the simple case of $\mathrm{PrTi_2Al_{20}}$. This experimental finding indicates that the excited CEF triplet states in the Zn-based materials have a more significant influence on the ordered structure than in the Al-based materials. The Γ_5 quadrupoles, O_{xy}, O_{yz}, and O_{zx}, become nonzero within the Γ_4 first-excited CEF state. O_{yz} and O_{zx} also accompany the induced $\boldsymbol{M}_\mathrm{AF}$ along the [0 0 1] axis under the $[\bar{1}10]$ magnetic fields, which is deduced from the invariant form in the free-energy function, $J_xJ_yO_{xy} + J_yJ_zO_{yz} + J_zJ_xO_{zx}$. The invariant form of $T_{xyz}(J_zO_{xy} + J_xO_{yz} + J_yO_{zx})$ allows coexistence of T_{xyz} and $O_{zx} - O_{yz}$ under the $[\bar{1}10]$ magnetic fields. These various multipoles can become finite through mixing of the Γ_3 and Γ_4 CEF levels. Such contributions of the excited levels to the multipole states were discussed for the Van Vleck-type quadrupole ordering in YbSb [32] and for the elastic softening anomaly in $\mathrm{PrMg_3}$ [33].

The above considerations finally yields the conclusion that O_2^2, T_{xyz}, O_{yz}, and O_{zx} can have nonzero magnitudes simultaneously. This multipole entanglement is expected to accompany an induced $\boldsymbol{M}_\mathrm{AF}$ which is almost parallel to the [1 1 1] axis, as shown in Fig. 4. Then, the structure factors are closer to the $F^2_{[111]}$ listed in Table I, which is in accordance with the experimental result.

D. Demonstration of multipole entanglement

Hereafter, we exemplify the ordering of such entangled multipoles by considering the full CEF levels. We simply employ a two-sublattice mean-field model with nearest-neighbor interactions. The Hamiltonian is expressed as

$$\begin{aligned}\mathcal{H} = \mathcal{H}_\mathrm{CEF} &+ K_3\big(\langle O_2^0\rangle O_2^0 + \langle O_2^2\rangle O_2^2\big)\\ &+ K_5(\langle O_{xy}\rangle O_{xy} + \langle O_{yz}\rangle O_{yz} + \langle O_{zx}\rangle O_{zx})\\ &+ K_\mathrm{O}(\langle T_{xyz}\rangle T_{xyz}) - g_J\mu_\mathrm{B}\boldsymbol{J}\cdot\boldsymbol{B}. \qquad (1)\end{aligned}$$

$\mathcal{H}_\mathrm{CEF}$ represents the CEF Hamiltonian for the $4f^2$ electron configuration of Pr^{3+}, for which the parameters in the disordered phase have already been determined by the INS study [19]. The K_3, K_5, and K_O parameters are the exchange interaction energies for the multipoles. $\langle O\rangle$ is the thermal average of the multipole-moment operator, O. The last term in Eq. (1) represents the Zeeman effect caused by the applied magnetic field, $\boldsymbol{B}$. Before considering the results, it should be mentioned that such a simple two-sublattice model with the nearest-neighbor interaction differs from the aforementioned ANNNI model that was suggested as being relevant to the ↑↑↓↓ stacking shown in Fig. 4. Moreover, the diamond-type Pr-ion sublattice with *fcc* symmetry frustrates the interactions, thereby resulting in more complex physics than that based on the simple two-sublattice model. However, this demonstration is helpful for consideration of the entangled multipoles.

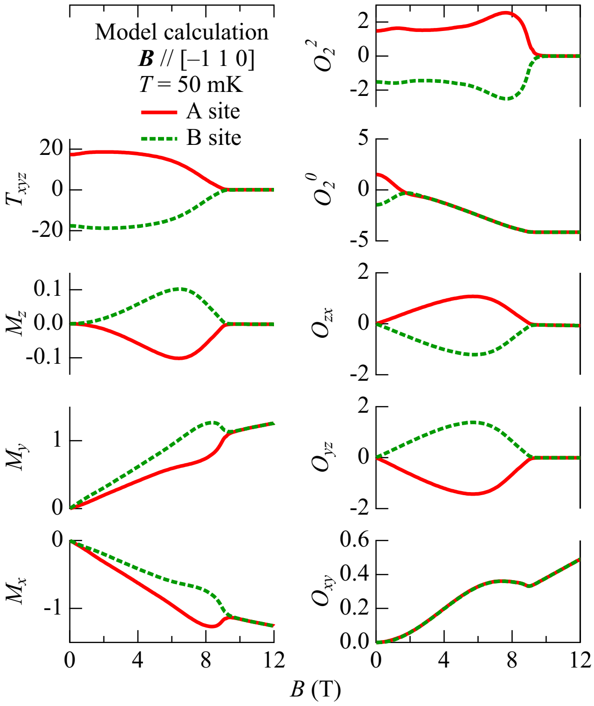

FIG. 6. Calculated magnitudes of multipole components as functions of a magnetic field applied parallel to the $[\bar{1}10]$ axis at 50 mK, based on the two-sublattice mean-field model defined by Eq. (1). The red solid line and green broken line indicate the two sublattices, A and B, respectively.

We have calculated the multipoles at 50 mK as functions of the magnetic field, as shown in Fig. 6. In order to reproduce the upper critical magnetic field for the actual phase diagram of $\mathrm{PrIr_2Zn_{20}}$ [21], we chose the parameter set of $K_3 = 0.0025$ meV, $K_5 = 0.0026$ meV, and $K_\mathrm{O} = 0.00011$ meV. This parameter set gives the critical magnetic field of 9 T applied parallel to the $[\bar{1}10]$ axis. An antiferromagnetic-type ordering due to the staggered moments at the A and B sites appears below the upper critical magnetic field of 9 T. On the other hand, the calculated $T_\mathrm{Q} = 0.5$ K is higher than the actual T_Q (0.11 K). This discrepancy is caused not only by the mean-field approximation, but also by the neglect of the frustration in the interactions that is expected from the low value of the magnetic entropy at T_Q.

The staggered order parameters are O_2^0, O_2^2, and T_{xyz} under zero-field conditions. With increasing magnetic field, O_2^0 is rapidly suppressed and staggered arrangements of $J_x(M_x), J_y(M_y), J_z(M_z), O_{yz}$, and O_{zx} are induced. The O_{xy} quadrupole does not exhibit an antiferromagnetic-type pattern. The staggered magnetic moments, $\boldsymbol{M} = (M_x, M_y, M_z)$, induced at 5 T and 50 mK, are $(-0.779, 0.502, -0.081)$ at the A site and $(-0.513, 0.769, 0.081)$ at the B site in units of μ_B/Pr, and, thus, the amplitudes of the AFM components are $\boldsymbol{M}_\mathrm{AF} = \pm(0.132, 0.133, 0.081)$. These induced AFM $\boldsymbol{M}_\mathrm{AF}$ are closer to the [1 1 1] direction than those for the pure O_2^2 case where the AFM vectors are parallel to the [1 1 0] direction.

In addition, we can compare the calculated results to the observed field-induced ferromagnetic component for the intensity at $\boldsymbol{Q} = (2,2,0)$ under the $[\bar{1}10]$ magnetic fields. The ferromagnetic component can be calculated as $(-M_x + M_y)/\sqrt{2}$ for each Pr-ion site. According to the calculated results shown in Fig. 6, these are approximately proportional to the magnetic field. Because the neutron-diffraction intensity is proportional to the squared magnitude of magnetic moment, the calculated result is consistent with the observed B^2 dependence of intensity shown in Fig. 1(d). This behavior also supports the nonmagnetic multipole ordering in $\mathrm{PrIr_2Zn_{20}}$.

For the structure factor calculations conducted here, we used the magnetic form factor of the Pr^{3+} ion based on the conventional dipole approximation [34]. Thus, the magnetization distribution inside the entangled multipole was neglected. In the case of $\mathrm{Ce_{0.7}La_{0.3}B_6}$, the intensities of the neutron superlattice reflections in the octupole ordered phase were explained by considering the magnetic form factor which takes a maximum value at a finite momentum transfer [3]. Such modification of the magnetic form factor owing to the internal magnetization is necessary in order to understand the measured result more precisely.

E. Relevance of entangled multipoles to electronic phenomena

As a consequence of the mean-field analysis, the staggered order of O_2^0 disappears at approximately 2 T. This behavior corresponds to the anomaly in the elastic constant between 1 and 2 T inside the ordered phase [21]. In addition, the octupole T_{xyz} and the induced quadrupoles O_{yz} and O_{zx} begin to decrease above 5 T, whereas O_2^2 increases from 5 to 6 T. This variation of the relative multipole weights within the ordered phase seems to correspond to the other elastic-constant anomaly at 6 T.

We have also calculated the ordered multipoles under the influence of the magnetic fields applied along the [0 0 1] axis, using the same set of the parameters in the Hamiltonian given in Eq. (1) ($K_3 = 0.0025$ meV, $K_5 = 0.0026$ meV, $K_\mathrm{O} = 0.00011$ meV, and the CEF parameters determined in the previous INS study [19]). The calculated upper critical field of the ordered phase is 6 T, which is close to the actual value of 5 T. This mean-field result shows the suppression of the AFQ order of O_2^0 and O_2^2 at approximately 3 T, which is accompanied by the disappearance of the induced AFM peak. It is also consistent with the experimental result that no superlattice peak is observed when fields of 1.5 and 3.5 T are applied along the [0 0 1] axis. This calculated suppression of the AFQ order may induce hump anomalies in the electrical resistivity between 2 and 3 T [24], along with anomalies in the elastic constants [21]. Therefore, the ordered phase of $\mathrm{PrIr_2Zn_{20}}$ is composed of various entangled multipoles, which are relevant at least to the two low-energy CEF levels.

As mentioned above and as shown in Fig. 4, the ordered structure is composed of a $\uparrow\uparrow\downarrow\downarrow$ stacking along the $\boldsymbol{c}_R$ axis of the ferro-type ordered planes. This structure is explained by the intersite interactions up to the second-nearest-neighbor sites along the stacking sequence [29] and means that the frustration of interactions plays a role in the ordered state. In addition, it should be noted that the Pr-ion sublattice has a diamond-type fcc symmetry, which is relevant to geometrical frustration for the antiferromagnetic-type nearest-neighbor interactions. Regarding the above-mentioned contributions of the various multipoles, the strong fluctuation of the electronic state is enhanced by such frustration effects. In other words, a short-range correlation may emerge at a temperature significantly higher than T_Q. This is consistent with the unusual release of the magnetic entropy, which is only 20% of that for the localized $4f$ electrons with the Γ_3 doublet state. Therefore, it is interesting to investigate diffuse scattering near the $\boldsymbol{q} = (1/2,1/2,1/2)$ positions, although the present experimental accuracy is not sufficient to resolve such a weak response.

We demonstrated the ordered structure of the entangled multipoles based on the mean-field calculation shown in Fig. 6. These entangled multipoles are also expected to correlate with the transport properties of $\mathrm{PrIr_2Zn_{20}}$ in the disordered phase, which is insisted to be caused by the two-channel Kondo effect. The Seebeck coefficient S/T at approximately 0.1 K increases from 0.03 $\mu\mathrm{V/K^2}$ near the zero magnetic field to 4.5 $\mu\mathrm{V/K^2}$ for a magnetic field of 5 T applied parallel to the [0 0 1] axis [24]. With increasing magnetic fields along the [0 0 1] axis, the NFL state changes to the Fermi-liquid state near 5 T. In addition, the elastic softening is enhanced under a magnetic field of 5 T [21]. Note that, recently, a theoretical work proposed a new electronic phase near 5 T, which is associated with the composite order of the itinerant and localized electronic states [10,35]. This composite order is caused by the two-channel Kondo effect associated with orbital-selective c-f interaction, which may vary with the magnetic-field tuning of relevant multipole fluctuations. The present structural investigation of the entangled multipoles is expected to shed light on these new attractive properties of $\mathrm{PrIr_2Zn_{20}}$. Namely, the magnetic-field tuning of the entangled multipoles and the fluctuations may cause the variations or the crossover phenomena in the electronic-correlation channel.

As already stated above, it has been suggested that the double phase transition at $T_\mathrm{Q} = 0.75$ K and $T^* = 0.65$ K of the isomorphic compound $\mathrm{PrV_2Al_{20}}$ is associated not only with the Γ_3-symmetry quadrupole ordering, but also with the ordering of the Γ_1-symmetry magnetic octupole T_{xyz}, both of which are finite within the Γ_3 CEF doublet ground state [13]. Considering the present neutron diffraction result revealing the role of T_{xyz} in the ordered state of $\mathrm{PrIr_2Zn_{20}}$, it seems promising to investigate the ordered phase of $\mathrm{PrV_2Al_{20}}$ within the various-multipole-ordering framework. The excited CEF triplet state in the Al-based 1-2-20 material contributes to the conventional magnetic Kondo effect in the higher-temperature range near 100 K, because the split energy corresponds to this temperature range. However, the triplet state does not play a role in the low-temperature ordering phase transitions in the Al-based materials, thereby the pure multipole orderings are expected to occur.

V. SUMMARY

In summary, a neutron diffraction experiment was conducted in this study, evidencing an antiferromagnetic-type multipole ordered structure below approximately 0.1 K in $\mathrm{PrIr_2Zn_{20}}$. The unit cell of the multipole order is characterized by $\boldsymbol{q} = (1/2,1/2,1/2)$ with respect to the structural cubic unit cell. The primary order parameter is the O_2^2 quadrupole, which becomes finite within the Kramers CEF doublet ground state. We also examined the multipole entanglement by including T_{xyz}, O_{yz}, and O_{zx}, which are attributed not only to the ground state, but also to the excited triplet states. The contributions of the various multipoles on the diamond-type Pr-ion sublattice are expected to produce strong electronic fluctuation which may cause gradual release of entropy up to a temperature one order of magnitude larger than T_Q. The variation of the multipole weights with the magnetic fields appears to be consistent with the observed anomalies, i.e., the softening of the elastic modulus, the dramatic enhancement of the Seebeck coefficient, and the hump anomalies in the electrical resistivity.

ACKNOWLEDGMENTS

We thank J.-L. Meuriot and P. Boutrouille for technical support for the low-temperature neutron-diffraction measurements. T. Masuda and M. Soda are acknowledged for their assistance with sample alignment through use of the high-energy x-ray diffraction technique at the Institute for Solid State Physics, The University of Tokyo. This study is supported in part by the Japan Society for the Promotion of Science (JSPS) KAKENHI Grant Numbers JP20102005, JP23102718 [Scientific Research on Innovative Areas "Heavy Electrons"], JP21224008 [Scientific Research (S)], JP23244068 [Scientific Research (A)], JP24654080 [Exploratory Research], JP26707017 [Grant-in-Aid for Young Scientists (A)], JP15H05886 [Scientific Research on Innovative Areas "J-Physics"], and JP15KK0169 [Fund for the Promotion of Joint International Research (Fostering Joint International Research)]. Support for the travel expenses incurred for the experiment performed at LLB was provided by the General User Program for Neutron Scattering Experiments of the Institute for Solid State Physics, The University of Tokyo. K.T.M. was supported by JSPS as a research fellow.

---

[1] J. M. Effantin, J. Rossat-Mignod, P. Burlet, H. Bartholin, S. Kunii, and T. Kasuya, J. Magn. Magn. Mater. **47–48**, 145 (1985).

[2] W. A. C. Erkelens, L. P. Regnault, P. Burlet, J. Rossat-Mignod, S. Kunii, and T. Kasuya, J. Magn. Magn. Mater. **63–64**, 61 (1987).

[3] K. Kuwahara, K. Iwasa, M. Kohgi, N. Aso, M. Sera, and F. Iga, J. Phys. Soc. Jpn. **76**, 093702 (2007).

[4] Y. Kuramoto, H. Kusunose, and A. Kiss, J. Phys. Soc. Jpn. **78**, 072001 (2009).

[5] P. Morin, D. Schmitt, and E. du Tremolet de Lacheisserie, J. Magn. Magn. Mater. **30**, 257 (1982).

[6] T. Onimaru, T. Sakakibara, N. Aso, H. Yoshizawa, H. S. Suzuki, and T. Takeuchi, Phys. Rev. Lett. **94**, 197201 (2005).

[7] R. Shiina, H. Shiba, and P. Thalmeier, J. Phys. Soc. Jpn. **66**, 1741 (1997).

[8] D. L. Cox and M. Jarell, J. Phys.: Condens. Matter **8**, 9825 (1996).

[9] T. Nasch, W. Jeitschko, and U. C. Rodewald, Z. Naturforschung **B 52**, 1023 (1997).

[10] T. Onimaru and H. Kusunose, J. Phys. Soc. Jpn. **85**, 082002 (2016).

[11] A. Sakai and S. Nakatsuji, J. Phys. Soc. Jpn. **80**, 063701 (2011).

[12] T. J. Sato, S. Ibuka, Y. Nambu, T. Yamazaki, T. Hong, A. Sakai, and S. Nakatsuji, Phys. Rev. B **86**, 184419 (2012).

[13] M. Tsujimoto, Y. Matsumoto, T. Tomita, A. Sakai, and S. Nakatsuji, Phys. Rev. Lett. **113**, 267001 (2014).

[14] A. Sakai, K. Kuga, and S. Nakatsuji, J. Phys. Soc. Jpn. **81**, 083702 (2012).

[15] K. Matsubayashi, T. Tanaka, A. Sakai, S. Nakatsuji, Y. Kubo, and Y. Uwatoko, Phys. Rev. Lett. **109**, 187004 (2012).

[16] K. Matsubayashi, T. Tanaka, J. Suzuki, A. Sakai, S. Nakatsuji, K. Kitagawa, Y. Kubo, and Y. Uwatoko, JPS Conf. Proc. **3**, 011077 (2014).

[17] R. Higashinaka, A. Nakama, M. Ando, M. Watanabe, Y. Aoki, and H. Sato, J. Phys. Soc. Jpn. **80**, SA048 (2011).

[18] K. Iwasa, R. Higashinaka, Y. Aoki, S. Ohira-Kawamura, and K. Nakajima, J. Phys. Soc. Jpn. **85**, 123704 (2016).

[19] K. Iwasa, H. Kobayashi, T. Onimaru, K. T. Matsumoto, N. Nagasawa, T. Takabatake, S. Ohira-Kawamura, T. Kikuchi, Y. Inamura, and K. Nakajima, J. Phys. Soc. Jpn. **82**, 043707 (2013).

[20] T. Onimaru, K. T. Matsumoto, Y. F. Inoue, K. Umeo, T. Sakakibara, Y. Karaki, M. Kubota, and T. Takabatake, Phys. Rev. Lett. **106**, 177001 (2011).

[21] I. Ishii, H. Muneshige, Y. Suetomi, T. K. Fujita, T. Onimaru, K. T. Matsumoto, T. Takabatake, K. Araki, M. Akatsu, Y. Nemoto, T. Goto, and T. Suzuki, J. Phys. Soc. Jpn. **80**, 093601 (2011).

[22] T. Onimaru, K. T. Matsumoto, Y. F. Inoue, K. Umeo, Y. Saiga, Y. Matsushita, R. Tamura, K. Nishimoto, I. Ishii, T. Suzuki, and T. Takabatake, J. Phys. Soc. Jpn. **79**, 033704 (2010).

[23] T. Onimaru, K. Izawa, K. T. Matsumoto, T. Yoshida, Y. Machida, T. Ikeura, K. Wakiya, K. Umeo, S. Kittaka, K. Araki, T. Sakakibara, and T. Takabatake, Phys. Rev. B **94**, 075134 (2016).

[24] T. Ikeura, T. Matsubara, Y. Machida, K. Izawa, N. Nagasawa, K. T. Matsumoto, T. Onimaru, and T. Takabatake, JPS Conf. Proc. **3**, 011091 (2014).

[25] A. Tsuruta and K. Miyake, J. Phys. Soc. Jpn. **84**, 114714 (2015).

[26] V. M. T. Thiede, W. Jeitschko, S. Niemann, and T. Ebel, J. Alloy. Comp. **267**, 23 (1998).

[27] E. Kroumova, M. I. Aroyo, J. M. Perez-Mato, A. Kirov, C. Capillas, S. Ivantchev, and H. Wondratschek, Phase Trans. **76**, 155 (2003).

[28] K. Momma and F. Izumi, J. Appl. Crystallogr. **41**, 653 (2008).

[29] P. Bak and J. von Boehm, Phys. Rev. B **21**, 5297 (1980).

[30] K. Hattori and H. Tsunetsugu, J. Phys. Soc. Jpn. **83**, 034709 (2014).

[31] H. Kusunose, J. Phys. Soc. Jpn. **77**, 064710 (2008).

[32] K. Hashi, H. Kitazawa, A. Oyamada, and H. A. Katori, J. Phys. Soc. Jpn. **70**, 259 (2001).

[33] K. Araki, Y. Nemoto, M. Akatsu, S. Jumonji, T. Goto, H. S. Suzuki, H. Tanida, and S. Takagi, Phys. Rev. B **84**, 045110 (2011).

[34] E. J. Lisher and J. B. Forsyth, Acta. Cryst. A **27**, 545 (1971).

[35] S. Hoshino, J. Otsuki, and Y. Kuramoto, J. Phys. Soc. Jpn. **82**, 044707 (2013).